Electronic supplementary information (ESI)

Hydrogen evolution across nano-Schottky junctions at carbon supported MoS_2 catalysts in biphasic liquid systems

Peiyu Ge,[a] Micheál D. Scanlon,[a] Pekka Peljo,[b] Xiaojun Bian,[c] Heron Vubrel,[d] Arlene O'Neill,[e] Jonathon N. Coleman,[e] Marco Cantoni,[f] Xile Hu,[d] Kyösti Kontturi,[b] BaoHong Liu[c] and Hubert H. Girault*[a]

[a]Laboratoire d'Electrochimie Physique et Analytique, Ecole Polytechnique Fédérale de Lausanne (EPFL), Station 6, CH-1015 Lausanne, Switzerland.

[b]Department of Chemistry, Aalto University, P.O. Box 16100, 00076, Finland.

[c]Department of Chemistry, Institute of Biomedical Sciences, Fudan University, Shanghai, 200433, P.R. China.

[d]Laboratory of Inorganic Synthesis and Catalysis, Ecole Polytechnique Fédérale de Lausanne, BCH-3305, CH-1015 Lausanne, Switzerland.

[e]School of Physics and Centre for Research on Adaptive Nanostructures and Nanodevices (CRANN), Trinity College Dublin, D2, Ireland.

[f] Interdisciplinary Centre for Electron Microscopy (CIME), Ecole Polytechnique Fédérale de Lausanne, Station 12, CH-1015, Lausanne, Switzerland.

Section S1: Synthesis and characterization of each MoS_2-based catalyst

Nanocrystalline molybdenum(IV) sulphide (MoS_2) with an average particle size of 6 µm (max. 40 µm) was purchased from Aldrich (catalogue number: 69860). XPS and TEM analysis of this material were reported by our group previously.[1] Exfoliated MoS_2 was prepared and characterized as reported previously by Coleman *et al*.[2]

Mesoporous carbon nanospheres were prepared according to Zhao's method.[3] Briefly, 0.3 g of phenol, 1.05 ml of formalin aqueous solution (37 wt %) and 7.5 ml of 0.1 M NaOH aqueous solution were mixed and stirred at 70 °C for 0.5 h. Then, 0.48 g of triblock copolymer Pluronic F127 dissolved in 7.5 ml of distilled water was added, and the mixture was stirred at 66 °C for 2 hours. After that, 25 ml of water was added to dilute the solution and stirred for another 18 hours. When the mixture was cooled down, 17.7 ml of the obtained solution and 56 ml of H_2O were transferred into an autoclave and kept at 130 °C for 24 hours. The mixture was centrifuged and washed with copious amounts of water and dried at 50 ^{0}C overnight. The final products were obtained after carbonization at 700 °C in a N_2 atmosphere for 3 hours.

MoS_2 on mesoporous carbon and MoS_2 on graphene materials were prepared using a one-step hydrothermal method identical to that described by Dai and co-workers.[4] 22 mg of $(NH_4)_2MoS_4$ and 10 mg mesoporous carbon or 10 mg graphene oxide in 10 mL DMF were dispersed by sonication to achieve a homogeneous solution. After that, 0.1 mL of $N_2H_4.H_2O$ was added and sonicated for 30 min. Next the reaction solution was transferred to a 40 mL autoclave and kept at 200 ^{0}C for 12 hours. The mixtures were centrifuged and washed with

water several times. The final products were obtained after several hours of lyophilization. For comparison, reduced graphene materials were obtained using the same synthesis process but without the addition of $(NH_4)_2MoS_4$.

Detailed characterisations of MoS_2 on graphene and MoS_2 on mesoporous carbon have been reported by the groups of Dai[4] and Liu,[5] respectively. Both the carbon supports (either graphene or mesoporous carbon) and the carbon supported MoS_2 catalyst nanoparticles had a homogeneous size distribution. For example, both mesoporous carbon and MoS_2 on mesoporous carbon nanoparticles have uniform diameters of 150 nm, as shown by scanning electron microscopy (SEM) images in Fig. S1 (a). High magnification SEM (Fig. S1 (b)) clearly shows MoS_2 uniformly decorating the surface of mesoporous carbon. In contrast, as reported,[4-5] in the absence of mesoporous carbon or graphene the freely grown MoS_2 particles coalesce into aggregated structures with various sizes hundreds of nanometers in diameter. High resolution transmission electron microscopy (HR-TEM) images as well as EDX analysis of MoS_2 on mesoporous carbon reveal that MoS_2 was grown on the mesoporous carbon surface with a layered structure of a few nanometers, see Fig. S1 (c, d, e). Identical observations were reported by Dai and co-workers[4] regarding MoS_2 growth on graphene . The HR-TEM images in Fig. S1(b) and those reported by Dai and co-workers[4] re-enforce the notion of how interconnected the MoS_2 and carbon supports are. This is a crucial factor in enhancing the electrocatalytic activity of these hybrid materials as discussed in the main text.

ICP analysis showed the molar ratio of C/Mo as about 10/1 for both MoS_2 on graphene and MoS_2 on mesoporous carbon.

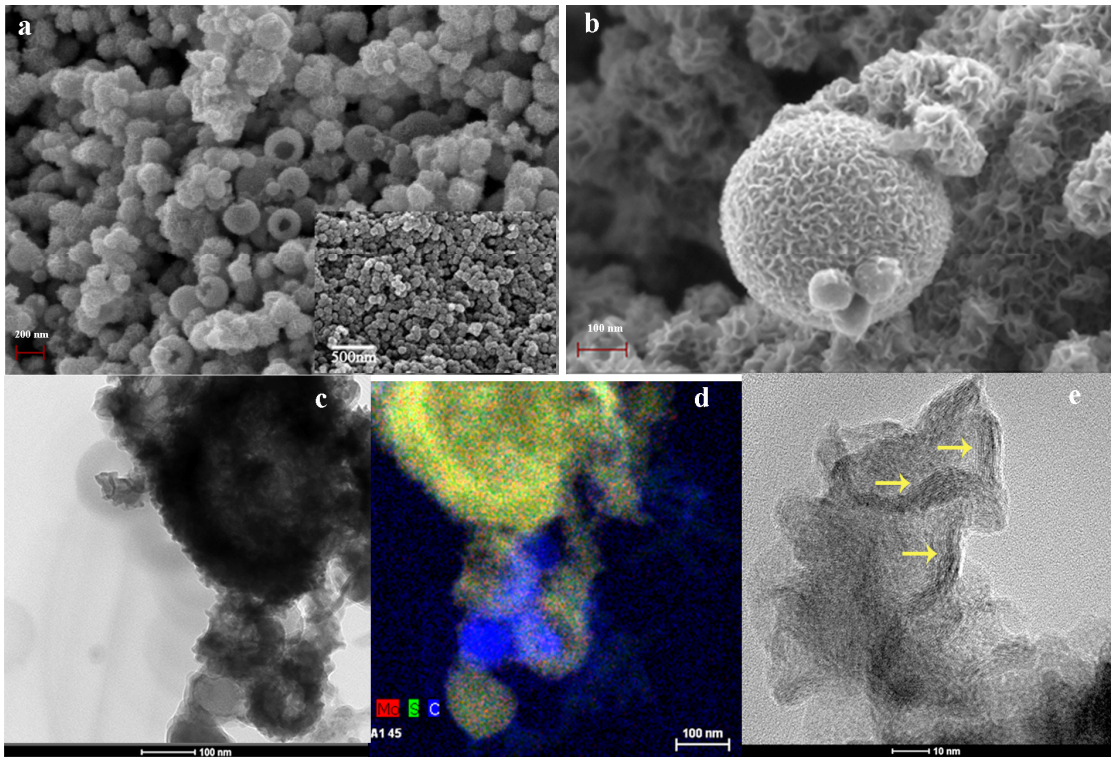

Fig. S1. (a) SEM image of MoS_2 on mesoporous carbon nanoparticles, magnification 28.6 k (Insert: SEM image of mesoporous carbon). (b) SEM image of MoS_2 on mesoporous carbon nanoparticles, magnification 101.5 k. (c) TEM image of MoS_2 on mesoporous carbon. (d) EDX analysis of MoS_2 on mesoporous carbon of fig. S1 (c), showing uniform coating of Mo and S on the carbon. (e) High resolution TEM of MoS_2 on mesoporous carbon (yellow arrows indicate the location of MoS_2).

Section S2: Analysis of the kinetics for the hydrogen evolution reaction (HER) in a biphasic system in the presence and absence of each of the MoS_2-based catalysts

UV/Vis spectra of the product of the biphasic reaction, decamethylferrocenium cation ($DMFc^+$), were measured on an Ocean Optics CHEM2000 spectrophotometer using a quartz cuvette with a path length of 10 mm, volume of 4 mL, and equipped with a teflon cap to prevent evaporation of the organic phase during analysis (see picture of cuvette in Fig. 1, main text). Decamethylferrocene (DMFc, ≥99% Alfa Aesar) was purified by vacuum sublimation at 140 °C.[6] 1 mL of a 1,2-DCE solution containing 2.5 mM of DMFc was mixed, in a quartz cuvette, with 1 mL of an aqueous solution containing 100 mM HCl and 10 mM LiTB in the presence and absence of 0.25 mM of one of the respective hydrogen evolution catalysts (it should be noted that the mass of MoS_2 was kept constant for each experiment, *i.e.* for each hybrid MoS_2-catalyst the w/w % of MoS_2 was determined based on the ICP analysis and the equivalent mass of 0.25 mM MoS_2 weighed out). Chemical control of the Galvani potential difference was achieved using TB^- as a common ion. The highly hydrophobic TB^- species, initially present in the aqueous phase, transfers into the organic phase thereby establishing a distribution potential. The interface is polarised positively, at approximately 0.55 V, thus promoting the transfer of aqueous protons to the organic phase with resultant HTB acid formation in 1,2-DCE. All UV/Vis spectroscopic experiments were completed using aqueous and organic solutions thoroughly de-gassed with nitrogen, under anaerobic conditions in a glove box purged with nitrogen, in the dark, and at an ambient temperature of 23

± 2 °C. UV/Vis scans were taken at regular intervals over a period of 30 mins. During scan intervals the solution in the cuvette was constantly agitated with a magnetic stirrer. A molar extinction coefficient (ε) of $DMFc^+$ in 1,2-DCE was determined previously to be 0.632 mM^{-1} cm^{-1}.[1]

None of the catalytic microparticles were aqueous or organic soluble, as described for MoS_2 previously.[1] Once the two phases were emulsified mechanically the microparticles sediment at liquid/liquid interface, irrespective of whether they were initially suspended in the aqueous or organic phase. The preferential adsorption of particles at the liquid/liquid interface is driven by the minimization of the interfacial free energy in the system.[7] The capture of particles at the ITIES is energetically favourable when the interfacial tension of two immiscible fluids is higher than the difference of the interfacial tension of the particle–aqueous phase and the particle–oil phase, respectively.[8]

The rate of reaction was found to be approximately first order in respect to DMFc by plotting the logarithm of the reaction rate (estimated by the derivate of the measured data between each measurement point) *vs.* the logarithm of DMFc concentration (Fig. S2(A)). The reaction order was found to be independent of the proton concentration when $[H^+] > 1$ mM.

Therefore, the rate of reaction can be written as

$$v = \frac{d[\mathrm{DMFc}^+]}{dt} = k[\mathrm{DMFc}] \qquad \text{(S1)}$$

where k is the apparent rate constant of the reaction. The integrated rate law was expressed as[9]

$$kt = \ln\frac{a}{a-x} \qquad \text{(S2)}$$

where *a* is the initial concentration of DMFc and *x* is the concentration of $DMFc^+$. The right hand side of equation S2 when plotted as a function of time gave a straight line with a slope of *k* (Fig. S2(B)). This method was used to calculate the rate constants for the reactions with different catalysts (Table 1). The calculated rate constants were used to plot the theoretical $DMFc^+$ concentration as a function of time in Fig. 1. A linear dependence, with $R > 0.996$ for equation S2, was observed when DMFc conversion was less than 80 %. The calculated rate constants are able to reproduce the experimental results, confirming that the assumed reaction rate equation corresponds with the experimental data (Fig. 1, Fig. S3).

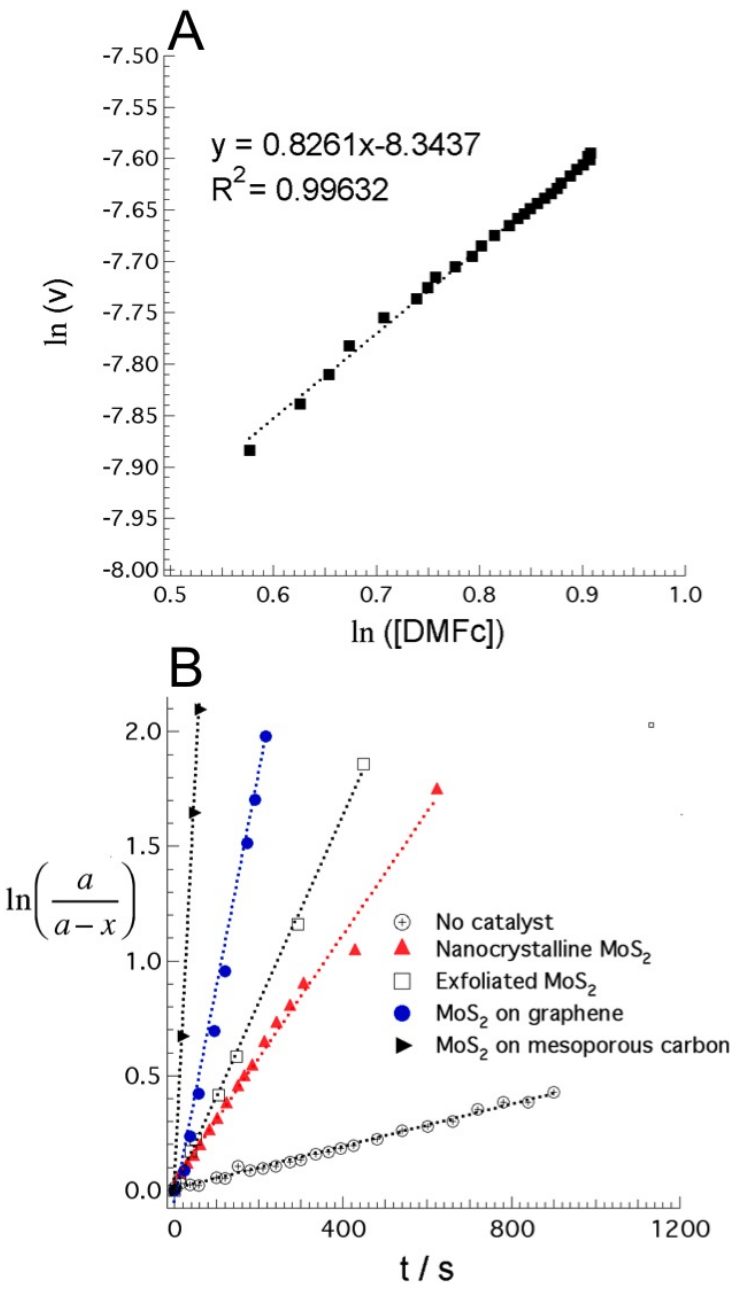

Fig. S2. **(A)** Natural logarithm of the reaction rate (mM s^{-1}), estimated from the derivate of the experimental data between each measurement point, as a function of the logarithm of DMFc concentration (mM) for the experiment without any catalyst. **(B)** Plot of the integrated rate law, see equation S2, where a is the initial concentration of DMFc and x is the concentration of $DMFc^+$, versus time (s). The slopes of the straight lines represent the rate constants (k / s^{-1}) for the reactions with different catalysts (as tabulated in table 1).

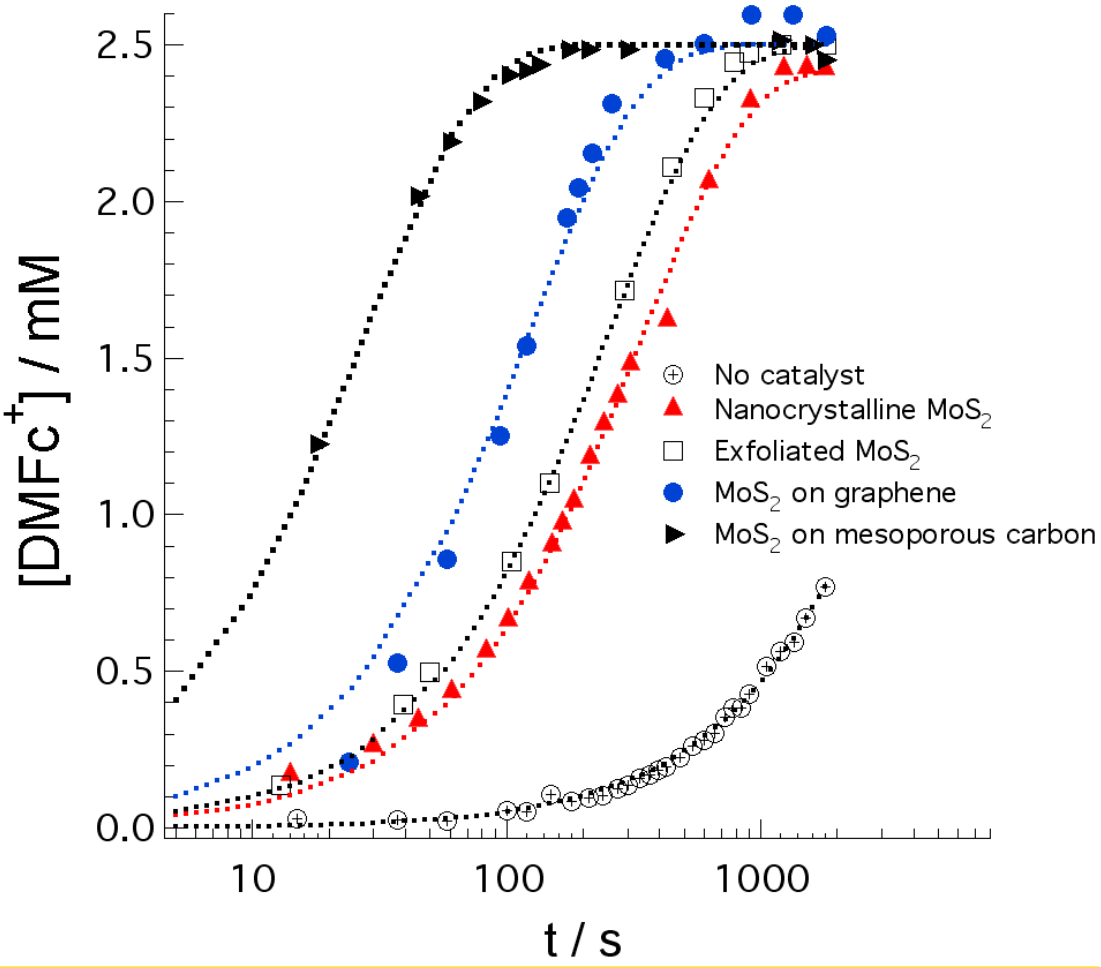

Fig. S3. The kinetics of the hydrogen evolution reaction (HER), in the absence and presence of each of the MoS_2 based catalysts, as followed by monitoring changes in the UV/Vis absorbance (λ_{max} = 779 nm) for $DMFc^+$ produced in a biphasic experiment, are clarified by using a logarithmic scale for the reaction time. Theoretical curves (dotted lines) were obtained from the calculated rate constants (k / s^{-1}, see table 1).

Section S3: Cyclic voltammetry studies at the liquid – liquid interface

Voltammetry experiments at the water/1,2-dchloroethane interface were performed in a four-electrode configuration using a PGSTAT potentiostat (Eco-Chemie, Netherlands). Two platinum counter-electrodes were positioned in the aqueous and organic phases, respectively, to supply the current flow. The external potential was applied by means of two reference electrodes, either silver/silver chloride (Ag/AgCl) or silver/silver sulphate (Ag/Ag_2SO_4), which were connected to the aqueous phase and 1,2-DCE phases, respectively, *via* a Luggin capillary as illustrated previously.[1] The area of the liquid/liquid interface was 1.53 cm^2. The electrochemical cell compositions studied are illustrated in Scheme S1. The Galvani potential difference across the interface was determined by assuming the formal ion-transfer potential of a tetraethylammonium cation (TEA^+) to be 0.019 V.[10] Bis(triphenylphosphoranylidene)ammonium tetrakis(pentafluorophenyl)borate (BATB) was prepared by metathesis of a 1 : 1 mixture of bis(triphenylphosphoranylidene)ammonium chloride (BACl, ≥98%, Fluka) with lithium tetrakis(pentafluorophenyl)borate diethyl etherate (LiTB, Aldrich) in a methanol/water mixture (2 : 1 v/v) and subsequent recrystallization in acetone.[11] All voltammetric experiments were completed using aqueous and organic solutions thoroughly de-gassed with nitrogen, under anaerobic conditions in a glove box purged with nitrogen, in the dark and at an ambient temperature of 23 ± 2 °C.

Scheme S1. Composition of electrochemical cell used for ion transfer voltammetry.

Anaerobic conditions were necessary to avoid side reactions with oxygen, such as H_2O_2 generation.[12] In the blank cell, the potential window was limited by H^+ and SO_4^{2-} transfer from water to DCE at the positive and negative ends, respectively (Fig. S4 (A), black CV). The more hydrophilic SO_4^{2-} was chosen instead of Cl^-, extending the potential window in the negative direction, and allowing ion transfer of $DMFc^+$ to be monitored. On addition of 1 mM DMFc to the organic phase, the onset potential of proton transfer at the positive end of the potential window decreased in comparison with the blank (Fig. S4 (A), blue CV). This indicated that an assisted proton transfer (APT) took place in the presence of DMFc under anaerobic conditions.[12b] However, in contrast to proton coupled electron transfer (PCET), observed for H_2O_2 generation by DMFc under aerobic conditions,[12a] the presence of a clear return peak in the back scan indicated the back transfer of protons from DCE to the water phase. Such a back transfer of protons may have arisen from a lack of chemical reactions whereby the proton, in the form of $DMFcH^+$, remained either unconsumed or consumed at a very slow rate in the organic phase. As summarised in Equation 2 in the main text, the expected reaction products of the interaction between DMFc and protons at the polarised liquid-liquid interface were H_2 and $DMFc^+$. Indeed, a small current wave, with a formal transfer potential ($\Delta_o^w\phi$) of ca. -0.26 V, attributable to $DMFc^+$

transfer was observed in the negative potential region. However, the small magnitude of this peak re-enforced the assumption that a slow chemical reaction was occurring in 1,2-DCE. From the voltammetry it may be surmised that, under anaerobic conditions and in the absence of catalyst, hydrogen evolution occurs in the presence of DMFc at a slow rate.

The influence of several MoS_2 based complexes; acting as interfacial H_2 evolution catalysts, on the voltammetric response for an electrochemical cell with 1 mM DMFc dissolved in the organic phase was investigated. On dispersion of nanocrystalline MoS_2 in the aqueous phase, at a concentration of 0.25 mM, the particles sediment at the interface and in particular at the oil-water-glass three phase junction, driven by the minimization of the interfacial free energy in the system. An increased current wave, typical of a PCET process, was clearly observed in the positive potential region occurring at an earlier onset potential than in the absence of catalyst, (Fig. S4 (A), green CV). Previously, this increased current was attributed to heterogenous H_2 production where the aqueous protons are reduced on interfacial MoS_2 particles, also contacting the organic electron donor. The formation of the hydride may not take place and instead protons may be adsorbed on the nanocrystalline MoS_2 particles, likely on the edges.[1]. The catalytic effect of nanocrystalline MoS_2 allowed the proton in the organic phase to undergo fast chemical reaction, become fully consumed (explaining the absence of a return peak for proton transfer) with resultant H_2 evolution and $DMFc^+$ formation. The increased magnitude of the $DMFc^+$ transfer current wave in the negative potential region, in comparison to the situation without a catalyst present, provided further evidence of the catalytic activity of nanocrystalline MoS_2 in this biphasic system.[1]

The catalytic influences of exfoliated MoS_2, MoS_2 on mesoporous carbon, and MoS_2 on graphene on the HER were studied simply by each replacing nanocrystalline MoS_2 in the electrochemical cell (Scheme S1). Initially, control experiments were performed with either 0.5 mM mesoporous carbon or 0.5 mM graphene dispersed in the aqueous phase and 1 mM DMFc in 1,2-DCE. In the presence of these particles large capacitive currents were obtained, indicating adsorption at the ITIES (CVs not shown). However, no PCET or increases in the $DMFc^+$ transfer current wave were noted, with no suggestion of catalytic H_2 evolution.

At a concentration of 0.25 mM large interfacial Marangoni instabilities[13] were observed in the presence of exfoliated MoS_2, MoS_2 on mesoporous carbon and MoS_2 on graphene within a defined potential region, -0.2 to 0.2 V (CVs not shown). As reported previously for nanocrystalline MoS_2,[1] the microparticles swirl violently on polarisation of the liquid/liquid interface. However, no interfacial Marangoni effects were observed in this instance, indicating that such movement does not disrupt the voltammetry. From the kinetics data we conclude that the rate of H_2 evolution is greater in the presence of exfoliated MoS_2, MoS_2 on mesoporous carbon and MoS_2 on graphene than with nanocrystalline MoS_2 as a catalyst or in the absence of a catalyst (Fig. 1 and Table 1, main text). Thus, in the presence of the more efficient catalysts an increased abundance of H_2 bubble nucleation sites may be present at the ITIES, *i.e.* a greater quantity of available MoS_2 edge sites. As a result, more H_2 bubble formation may occur, with a resultant increase in disruption of the ITIES, leading to the observed instabilities. In the presence of MoS_2 on mesoporous carbon, for example, the H_2 bubble formed within 3-4 scans of the potential window. This

bubble quickly reformed at the interface, after removal of the former, indicative of rapid H_2 evolution.

Dilution of the catalyst concentration dispersed in the aqueous phase, with an expected decrease in H_2 bubble formation, was necessary in order to observe the voltammetric behaviour of exfoliated MoS_2, MoS_2 on mesoporous carbon and MoS_2 on graphene without interfacial instabilities. Exfoliated MoS_2 was diluted to a concentration of 0.1 mM. As observed in Fig. S4 (A) (red CV), despite dilution of the catalyst, the magnitude of the $DMFc^+$ transfer current wave in the negative potential region increased in comparison to that for nanocrystalline MoS_2 and a similar PCET current was observed in the positive potential region. These observations indicate that exfoliated MoS_2 is a superior H_2 evolution catalyst to nanocrystalline MoS_2.

The voltammetric responses for aqueous dispersions of MoS_2 om mesoporous carbon and MoS_2 on graphene in the electrochemical cell were broadly similar. Thus, solely a detailed examination of the MoS_2 on mesoporous carbon response will be presented herein. A 10 times dilution of dispersed MoS_2 on mesoporous carbon to 0.02 mM allowed clear CVs, free of Marangoni instabilities, to be obtained (Fig. S4 (B)). A larger capacitive current was observed in the presence of 0.02 mM MoS_2 on mesoporous carbon than 0.25 mM nanocrystalline MoS_2 due to the former strongly adsorbing at the ITIES. As before, a PCET process in the positive potential range and a large current wave in the negative potential range, corresponding to $DMFc^+$ transfer, confirmed MoS_2 on mesoporous carbon's ability to catalyse the HER in the presence of DMFc. CVs were also obtained in the presence of 0.1 mM MoS_2 on mesoporous carbon (Fig. S4 (B)). Increases in the capacitive and PCET currents were observed, once more

indicating the strong adsorption of MoS_2 on mesoporous carbon to the ITIES and also the ability of an increased catalyst concentration to accelerate the rate of reaction. The very large PCET current observed, greater than that for an identical concentration of exfoliated MoS_2 (0.1mM) and 0.25 mM nanocrystalline MoS_2, corroborated the kinetics data indicating that, of the catalysts studied for the HER, MoS_2 on mesoporous carbon is optimal. However, background subtraction revealed that the increase in current due to PCET did not increase proportionally with the catalyst concentration and no current increase due to $DMFc^+$ transfer was observed. On close inspection of the CVs in Fig. S4 (B) for MoS_2 on mesoporous carbon a small peak is evident at 0.2 V on the forward sweep. This peak may indicate adsorption at the ITIES (as also inferred by the large capacitance observed). The formation of an adsorption layer inhibits ion transfer at the interface. For example, TEA^+ transfer was only observed for low concentrations of MoS_2 on mesoporous carbon (0.02 mM). Consequently, it is reasonable to assume that a portion of $DMFc^+$ transfer is blocked thereby explaining the lack of a current increase in the negative potential region with increasing catalyst concentration.

In summary, the catalytic effect of the MoS_2-based particles allowed the transferred protons (from water to organic) to undergo a fast chemical reaction such that they became fully consumed, with resultant H_2 evolution and $DMFc^+$ formation, as summarised in equation 2 (main text).[1] The increased rate of proton consumption in the presence of each MoS_2-based catalyst was highlighted by (a) the observation of an increased current wave, occurring at an earlier onset potential than in the absence of catalyst, in the positive potential region typical of a PCET process, (b) by the absence of a

return peak for proton transfer from the organic to aqueous phase and (c) the increased magnitudes of the $DMFc^+$ transfer current wave in the negative potential region, in comparison to the situation without a catalyst present (Fig. S4 (A)). In the presence of the most efficient catalysts (exfoliated MoS_2, MoS_2 on mesoporous carbon and MoS_2 on graphene) extensive H_2 bubble formation occurred at the ITIES leading to the major Marangoni instabilities in the voltammetry. Indeed, dilution of the catalyst concentration dispersed in the aqueous phase was necessary in order to observe the voltammetric behaviour of exfoliated MoS_2, MoS_2 on mesoporous carbon and MoS_2 on graphene without interfacial instabilities (Fig. S4 (B)).

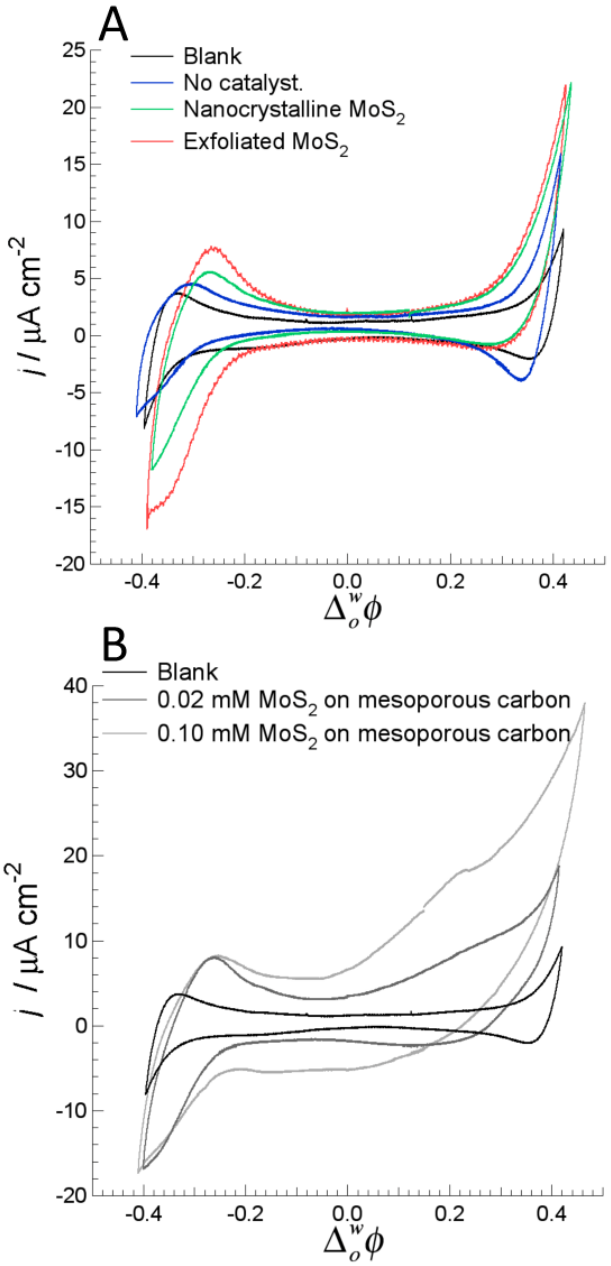

Fig. S4. Cyclic voltammograms (CVs) were obtained under anaerobic conditions, at a scan rate of 50 mV s^{-1}, using the electrochemical setup detailed in Scheme S1. **(A)** CVs are compared for a blank cell in the absence of both DMFc and catalyst; with 1 mM DMFc in 1,2-DCE; and with 1 mM DMFc in 1,2-DCE and either 0.25 mM nanocrystalline MoS_2 or 0.1 mM exfoliated MoS_2 in the aqueous phase. **(B)** CVs on dilution of the MoS_2 on mesoporous carbon catalyst concentration in the aqueous phase to 0.02 and 0.1 mM , respectively, and 1 mM DMFc in 1,2-DCE.

Section S4: Zeta (ζ)-potential and particle size measurements

Zeta (ζ)-potential measurements were carried out on a Nano ZS Zetasizer (Malvern Instruments, U.K.), with irradiation (λ = 633 nm) from a He-Ne laser, using Dispersion Technology Software (DTS). Each particle suspension (typically 0.7 – 1 mg / 5 ml) was initially dispersed in an aqueous NaOH solution, pH 12, and sonicated for at least 15 minutes to ensure a uniform dispersion free of any agglomerated particles. The pH was subsequently adjusted incrementally, while stirring, to pH 2 by dropwise addition of 0.5 M HCl and monitored using a Metrohm 632 pH meter. Samples (approximately 0.75 mL) were injected at regular pH intervals into a folded capillary cell and the drift velocity (ν) of the particles moving in an applied electric field (E), *i.e.* the electrophoretic mobility (μ) where μ = ν/E, was measured using a combination of electrophoresis and Laser Doppler Velocimetry (LDV) techniques.[14] Small frequency shifts (Δf) in the scattered light arising from movement of the particles through the crossover region of two coherent laser beams, arranged perpendicular to each other, were used to calculate μ from

$$\Delta f = \frac{2\nu \sin(\theta/2)}{\lambda} \qquad \text{(S3)}$$

where θ is the scattering angle. The ζ-potential (V) is elucidated from the measured electrophoretic mobility using Henry's equation,[14-15]

$$\zeta = \frac{3\eta\mu}{2\varepsilon}\frac{1}{f(\kappa a)} \qquad \text{(S4)}$$

where η is the solution viscosity and ε is the solution permittivity ($\varepsilon = \varepsilon_r\varepsilon_0$). $f(\kappa a)$ is Henry's function where κ^{-1} is the Debye length and a is the curvature radius of the charged particle. Henry's function takes into account effects associated with

particle size and the ionic strength of the solution. The function varies smoothly form 1 to 1.5 as κa varies from 0 to ∞.[16] For polar solvents, it is usually assumed that κa is large and that the particle radius is much larger than the double-layer thickness, so $f(\kappa a) \approx 1.5$, and Henry's equation simplifies to

$$\zeta = \frac{\eta \mu}{\varepsilon} \qquad \text{(S5)}$$

which is known as the Smoluchowski approximation.[14, 17] Smoluchowski's theory is valid for any shape of a particle provided $\kappa a \gg 1$.[14] All ζ-potential measuremnets were carried out at 25°C and a 2 min. equilibration time employed.

Size measurements were carried out using the Nano ZS Zetasizer by employing Dynamic Light Scattering (DLS). DLS measures Brownian motion and relates the particles speed to its size using the Stokes-Einstein equation (see Table S1). The particles were illuminated with the laser and the intensity fluctuations of the scattered light analyzed. In essence, if a large particle is being analyzed then intensity fluctuations occur slowly as the particle moves slowly. Particle size analysis by DLS determines the size for an equivalent spherical diameter particle, and hence the values reported herein are best interpreted as relative trends in aggregation rather than quantitative diameters. All particle size measurements were carried out at 25°C and a 2 min. equilibration time employed.

Directly measuring the surface charge of a particle for real systems is not possible. Whereas direct measurement of the ζ-potential is also not possible, this difficulty may be overcome by probing the charge of the surrounding ionic "atmosphere" in the immediate vicinity of the particles surface. A layer of tightly

bound ions of opposite charge, often called counter-ions, are present at the surface of a particle (Stern layer). These counter-ions are themselves in turn surrounded by a more diffuse zone of ions of the same charge as the particle, known as co-ions (Diffuse layer). The ζ-potential may thus be defined as the electrostatic potential difference between an average point at the layer of tightly bound counter-ions, *i.e.* at the hydrodynamic shear or slipping plane, and in the bulk.[14] The ζ-potential is a function of the charge density at the shear plane, whereas the surface potential is a function of the surface charge density. Other factors that influence ζ-potential are the nature of the surface, the electrolyte concentration in the solution, and the nature of the electrolyte and of the solvent.[14] The magnitude of the ζ-potential is almost always much smaller than the surface potential, however, it is still clearly a measure of the surface charge. The magnitude of the measured ζ-potential compared to the true surface potential depends on the Debye double layer thickness. High levels of ions in solution compress the double layer and the potential curve resulting in a measured ζ-potential only a fraction of the surface potential.[14] Thus, the accessible pH range of the zetasizer is restricted between pH 2 – 12.

For electrostatic reasons, colloidal particles with absolute ζ-potentials >15 mV are expected to be stable. Indeed, exfoliated MoS_2, MoS_2 on graphene, and MoS_2 on mesoporous carbon, each of which exhibited significantly negative ζ-potentials, disperse easily in water over the pH range studied using the zetasizer. However, between pH 2 to 2.3 each of these dispersions destabilized with resultant agglomeration formation and sedimentation. This was highlighted by analysis of the particle size distributions, with peaks of significant intensity attributable to irreversibly agglomerated particles observed at pHs ≤ 2.3 (Table

S1). At such high salt concentrations, the double layer collapses to the extent that the ever-present attractive van der Waals forces overcome the charge repulsion. This is an example of the so-called "salting out" effect. It is worth noting that agglomeration may also occur when the isoelectric point of a species is reached, as for nanocrystalline MoS_2 at pH 3.1, although no significant agglomeration was observed in this case at pH 2.56 (Table S1).

For MoS_2 on mesoporous carbon and MoS_2 on graphene an alternative explanation for the large negative ζ-potentials observed in Fig. 2 in the main text may be an increase in the abundance of negatively charged, hydrophilic oxygen-containing functional groups at their surfaces due to the oxidizing temperatures (200°C for 12 hours) employed during synthesis (Section S1). However, Dai and co-workers[4] report that residual oxygen is less than 4 atom % indicating that sulphur alone must be responsible for the negative charges.

Table S1. Comparison of the particle sizes of each MoS_2-based catalyst as determined using a Zetasizer Nano ZS.

Catalyst	Particle size distribution (% intensity, Zetasizer) nm
Nanocrystalline MoS_2	583.9 (100 %) @ pH 5.40 549.9 (100 %) @ pH 2.56
Exfoliated MoS_2	456.5 (100 %) @ pH 5.86 517.0 (90%) & 5023 (10%) @ pH 1.99
MoS_2 on graphene	774.6 (100 %) @ pH 5.03 734.3 (41%) & 3144 (59%) @ pH 2.30
MoS_2 on mesoporous carbon	155.8 (100 %) @ pH 5.85 200.9 (24%) & 900.1 (76%) @ pH 1.98

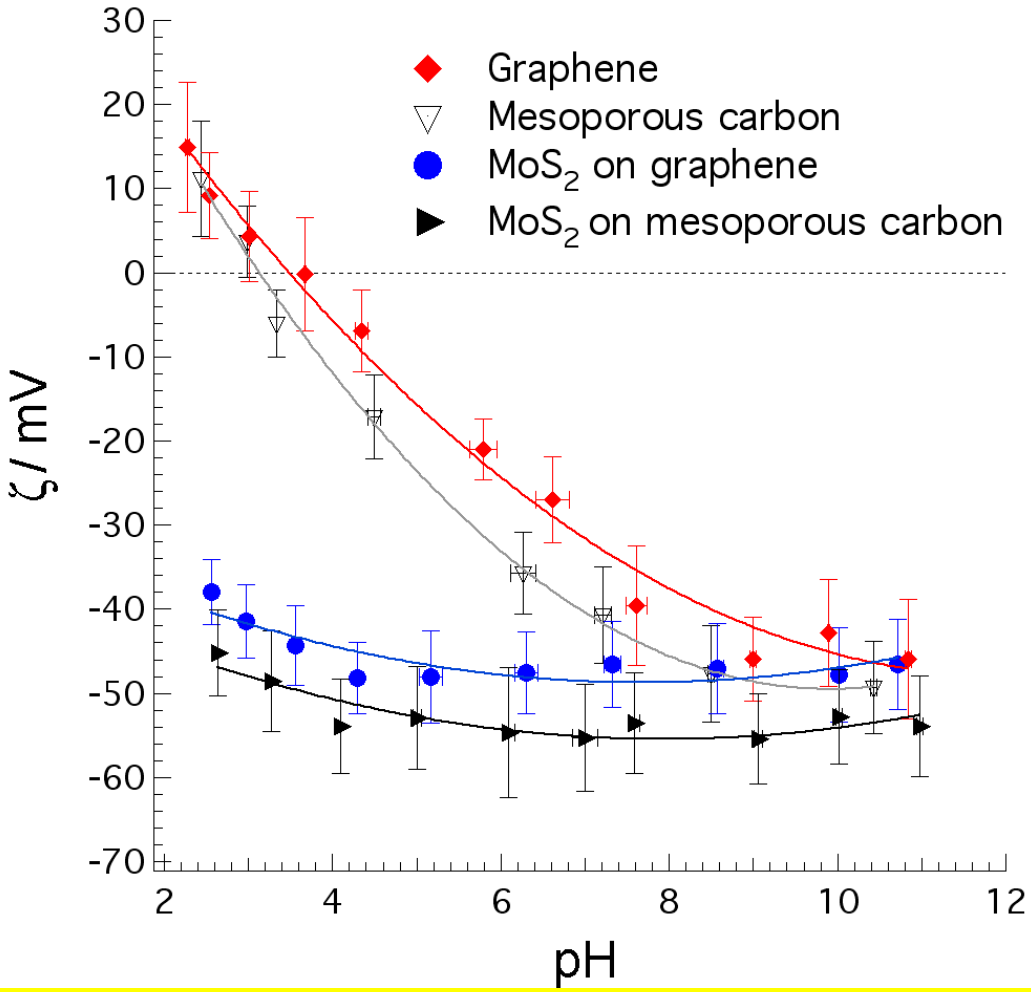

Fig. S5. Changes to the surface properties of graphene and mesoporous carbon on modification with MoS_2. Zeta (ζ)-potential measurements (mV) of graphene, mesoporous carbon, MoS_2 on graphene and MoS_2 on mesoporous carbon as a function of pH in aqueous dispersions at a concentration of 0.7 – 1 mg / 5 ml. The error bars in the y-direction represent the st. dev. of the ζ distribution around the mean result. The error bars in the x-direction represent the st. dev. of the change in pH before and after the ζ-measurements were obtained. The observed isoelectric points for mesoporous carbon (pI ≈ 3)[18] and graphene (pI ≈ 3.8)[19] are in agreement with the literature values.

Section S5: Band position calculations for MoS_2

Initially proposed by Butler and Ginley,[20] and more recently popularised by the paper of Xu and Schoonen,[21] the valence band edge (E_{VB}) at the semiconductor/electrolyte interface may be predicted from the electronegativity of the semiconductor using equation S6. The bulk electronegativity (χ) of a compound (M_aX_b) may be defined as the geometric mean of the electronegativities of the constituent atoms.[22] In turn, Mulliken[23] predicts that the absolute electronegativity of each constituent atom may be deduced from the electron affinity (EA) and ionisation potential (IP) of that atom using equation S7.

$$E_{VB} = (\chi_M^a \chi_X^b)^{1/(a+b)} + \tfrac{1}{2} E_g + 0.059(\mathrm{pH}_{zpc} - \mathrm{pH}) - E^e \qquad \text{(S6)}$$

$$\chi_M = \tfrac{1}{2}(\mathrm{IP}_M + \mathrm{EA}_M) \qquad \text{(S7)}$$

where χ_M and χ_X are the absolute electronegativities of the atoms X and M, respectively, E^e is the energy of free electrons on the hydrogen scale (ca. 4.5 eV) and E_g is the band gap of the semiconductor. Equation S6 simplifies to equation S8 at the point of zero charge, and the conduction band edge (E_{CB}) can be deduced from equation S9.

$$E_{VB} = \chi + \tfrac{1}{2} E_g - E^e \qquad \text{(S8)}$$

$$E_{CB} = E_{VB} - E_g \qquad \text{(S9)}$$

The IP and EA of molybdenum (Mo) are 7.10 and 0.746 eV, respectively.[24] The IP and EA of suphur (S) are 10.36 and 2.08 eV, respectively.[24a, 24c] From this data, using the equations above, we deduced that the absolute electronegativities of

Mo and S were 3.9 and 6.22 eV, respectively, and that the electronegativity of MoS_2 is 5.32 eV. Thus, applying equations S8 and S9 and knowing the band gap for MoS_2 to be 1.17 eV,[25] the top of the VB and bottom of the CB are calculated to be 0.235 and 1.405 eV with respect to the saturated hydrogen electrode (SHE), respectively.

To complete the reaction scheme illustrated in Fig. 3 in the main paper the literature values for the work function of graphene (0.1 eV vs. SHE),[26] the redox potential of the $DMFc^+$/DMFc couple in 1,2-dichloroethane (0.07 eV vs. SHE),[11] and the redox potential of the $H^+/½H_2$ redox couple both in an aqueous solution (0 eV vs. SHE)[27] and in 1,2-dichloroethane (0.55 eV vs. SHE)[12b] were used. It is worth noting that often in the literature the positions of energy levels are expressed on the absolute vacuum energy scale (AVS). Such band positions may be represented relative to the saturated hydrogen electrode (SHE) using equation S10.

$$E_{(SHE)} = -E_{(AVS)} - E^e \qquad \text{(S10)}$$

References

1. I. Hatay, P. Y. Ge, H. Vrubel, X. Hu and H. H. Girault, *Energy Environ. Sci.*, 2011, **4**, 4246-4251.
2. J. N. Coleman, M. Lotya, A. O'Neill and S. D. Bergin, *et al., Science*, 2011, **331**, 568-571.
3. Y. Fang, D. Gu, Y. Zou, Z. Wu, F. Li, R. Che, Y. Deng, B. Tu and D. Zhao, *Angew. Chem. Int. Ed.*, 2010, **49**, 7987-7991.
4. Y. Li, H. Wang, L. Xie, Y. Liang, G. Hong and H. Dai, *J. Am. Chem. Soc.*, 2011, **133**, 7296-7299.
5. X. Bian, J. Zhu, L. Liao, M. D. Scanlon, P. Y. Ge, C. Ji, H. H. Girault and B. H. Liu, *In preparation*, 2012.
6. A. Zahl, R. van Eldik, M. Matsumoto and T. W. Swaddle, *Inorg. Chem.*, 2003, **42**, 3718-3722.
7. (a) H. Duan, D. Wang, D. G. Kurth and H. Möhwald, *Angew. Chem. Int. Ed.*, 2004, **43**, 5639-5642; (b) W. H. Binder, *Angew. Chem. Int. Ed.*, 2005, **44**, 5172-5175; (c) D. Wang, H. Duan and H. Mohwald, *Soft Matter*, 2005, **1**, 412-416.
8. (a) Y. Lin, H. Skaff, T. Emrick, A. D. Dinsmore and T. P. Russell, *Science*, 2003, **299**, 226-229; (b) M. M. Gudarzi and F. Sharif, *Soft Matter*, 2011, **7**, 3432-3440.
9. P. W. Atkins. Physical Chemistry. 4th ed. Oxford: Oxford University Press, 1990.
10. T. Wandlowski, V. Mareček and Z. Samec, *Electrochim. Acta*, 1990, **35**, 1173-1175.
11. N. Eugster, D. J. Fermín and H. H. Girault, *J. Phys. Chem. B*, 2002, **106**, 3428-3433.
12. (a) B. Su, R. P. Nia, F. Li, M. Hojeij, M. Prudent, C. Corminboeuf, Z. Samec and H. H. Girault, *Angew. Chem. Int. Ed.*, 2008, **47**, 4675-4678; (b) I. Hatay, B. Su, F. Li, R. Partovi-Nia, H. Vrubel, X. Hu, M. Ersoz and H. H. Girault, *Angew. Chem. Int. Ed.*, 2009, **48**, 5139-5142.
13. (a) T. Kakiuchi, *J. Electroanal. Chem.*, 2002, **536**, 63-69; (b) Y. Kitazumi and T. Kakiuchi, *Langmuir*, 2009, **25**, 10829-10833; (c) L. Zhang, Y. Kitazumi and T. Kakiuchi, *Langmuir*, 2011, **27**, 13037-13042.
14. A. V. Delgado, F. González-Caballero, R. J. Hunter, L. K. Koopal and J. Lyklema, *Pure Appl. Chem.*, 2005, **77**, 1753-1805.
15. D. C. Henry, *Proc. R. Soc. London*, 1931, **A133**, 106-129.
16. B. M. Michov, *Electrophoresis*, 1988, **9**, 199-200.
17. M. Von Smoluchowski. Handbuch der Electrizität und des Magnetismus (Graetz). Leipzig: Barth, 1921:366.
18. (a) D. D. Asouhidou, K. S. Triantafyllidis, N. K. Lazaridis, K. A. Matis, S.-S. Kim and T. J. Pinnavaia, *Micro. Meso. Mater.*, 2009, **117**, 257-267; (b) L. Ji, F. Liu, Z. Xu, S. Zheng and D. Zhu, *Environ. Sci. Technol.*, 2010, **44**, 3116-3122; (c) F. Liu, Z. Xu, H. Wan, Y. Wan, S. Zheng and D. Zhu, *Environ. Toxicol. Chem.*, 2011, **30**, 793-800.
19. D. Li, M. B. Müller, S. Gilje, R. B. Kaner and G. G. Wallace, *Nat. Nanotechnol.*, 2008, **3**, 101-105.
20. (a) M. A. Butler and D. S. Ginley, *J. Electrochem. Soc.*, 1978, **125**, 228-232; (b) D. S. Ginley and M. A. Butler, *J. Electrochem. Soc.*, 1978, **125**, 1968-1974.

21. Y. Xu and M. A. A. Schoonen, *Am. Mineral.*, 2000, **85**, 543-556.
22. A. H. Nethercot Jr., *Phys. Rev. Lett.*, 1974, **33**, 1088-1091.
23. R. S. Mulliken, *J. Chem. Phys.*, 1934, **2**, 782-793.
24. (a) C. E. Moore, *Nat. Stand. Ref. Data Ser. (Nat. Bur. Stand., U.S., 1970)*, 1970, NSRDS-NBS 34; (b) C. S. Feigerle, R. R. Corderman, S. V. Bobashev and W. C. Lineberger, *J. Chem. Phys.*, 1981, **74**, 1580-1598; (c) H. Hotop and W. C. Lineberger, *J. Phys. Chem. Ref. Data*, 1985, **14**, 731-750.
25. (a) S. M. Ahmed, *Electrochim. Acta*, 1982, **27**, 707-712; (b) J.-L. Sculfort and J. Gautron, *J. Chem. Phys.*, 1984, **80**, 3767-3773.
26. (a) H. Hibino, H. Kageshima, M. Kotsugi, F. Maeda, F. Z. Guo and Y. Watanabe, *Phys. Rev. B*, 2009, **79**, 125437; (b) Y.-J. Yu, Y. Zhao, S. Ryu, L. E. Brus, K. S. Kim and P. Kim, *Nano Lett.*, 2009, **9**, 3430-3434.
27. H. H. Girault. Analytical and Physical Electrochemistry. Lausanne: EPFL Press, 2004.